Glycopolymeric Nanoparticles Block Breast Cancer Growth by Inhibiting Efferocytosis in the Tumor Microenvironment

Oluwaseyi Shofolawe-Bakare[1], Veeresh B. Toragall[2], Kenneth Hulugalla,[3] Railey Mayatt,[4] Paige Iammarino,[5] John P. Bentley,[6] Adam E. Smith[1,2], Thomas Werfel[1,2,3,7*]

[1]Department of Chemical Engineering, University of Mississippi, University, MS, USA, 38677

[2]Department of Biomedical Engineering, University of Mississippi, University, MS, USA, 38677

[3]Department of BioMolecular Sciences, University of Mississippi, University, MS, USA, 38677

[4]Department of Chemistry, Mississippi State University, Starkville, MS, USA. 39762

[5]Institute for Imaging and Analytical Technologies, Mississippi State University, Starkville, MS, USA, 39762

[6]Department of Pharmacy Administration, University of Mississippi, University, MS, USA, 38677

[7]Cancer Center and Research Institute, University of Mississippi Medical Center, Jackson, MS, USA, 39216

*Corresponding Author

Email: tawerfel@olemiss.edu

Abstract

Conventional inhibitors of immune checkpoints such as anti-programmed death-1 and its ligand (anti-PD-1/PD-L1) and anti-cytotoxic T lymphocyte-associated protein 4 (anti-CTLA4) have revolutionized therapeutic approaches to cancer, establishing immunotherapy as the standard of care for many cancers. A significant number of cancers, however, remain refractory to the inhibition of these immune checkpoints, leading to the search for alternative immune checkpoints that are more relevant to those diseases. Tumor-associated macrophage (TAM)-mediated

efferocytosis is an increasingly appreciated immune checkpoint with a profound impact on the phenotype of the tumor microenvironment (TME). TAMs perform their efferocytic function through the receptor MerTK, and MerTK activity correlates with tumor progression. To combat efferocytosis in the TME, we developed poly[[2-(diisopropylamino)ethyl methacrylate]-*b*-poly(methacrylamidomannose)] nanoparticles (PMAM NPs) capable of encapsulating and preferentially delivering UNC2025 (a MerTK inhibitor) to TAMs. The NPs had suitable physicochemical properties, such as a size of 130 nm and a neutral surface charge. The PMAM NPs encapsulated hydrophobic cargo and released them in a pH-dependent manner, showing suitability for cytosolic delivery. Moreover, the PMAM NPs showed 12-fold greater macrophage internalization than traditional PEGMA NPs. Macrophage internalization was shown to be dependent on the mannose receptor CD206, as the blockade of CD206 led to a significant decrease in PMAM NP internalization. Furthermore, PMAM NPs had a lower internalization than PEGMA NPs in 4T1 cancer cells that do not express CD206, further confirming macrophage selectivity. *In vivo* biodistribution studies showed the PMAM NPs were capable of internalization by TAMs in the TME. Lastly, UNC2025-PMAM NPs significantly reduced tumor volume compared to free UNC2025, showing greater therapeutic efficacy in a model of triple-negative breast cancer. These glycopolymer-based, efferocytosis-blocking NPs have promise both as a class of standalone cancer immunotherapy and as an adjuvant to improve response rates to checkpoint immunotherapy.

Keywords: Glycopolymer, Drug Delivery, Tumor-Associated Macrophages, Cancer Immunotherapy, Efferocytosis

1. Introduction

During tumorigenesis, tumors acquire a variety of mechanisms by which they dampen the adaptive immune response and consequently evade elimination.[1] These mechanisms are usually referred to as immune checkpoints.[2] The inhibition of prominent immune checkpoints such as programmed death ligand 1 (PD-L1) and cytotoxic T-lymphocyte associated protein 4 (CTLA-4) has revolutionized cancer treatment, greatly improving therapeutic outcomes in numerous cancers.[3,4] However, many cancers have an immunologically 'cold' phenotype, characterized by a paucity of T cells, and remain refractory to the inhibition of T cell checkpoints, driving the search for alternative immune checkpoints that can augment therapeutic efficacy in these diseases.[5,6]

Efferocytosis has recently emerged as a powerful immune checkpoint capable of rendering the tumor microenvironment (TME) unfavorable for cytotoxic T lymphocyte (CTL)-mediated antitumor immunity and contributing to chemoresistance.[7,8] Efferocytosis involves the eradication of apoptotic cells by phagocytes.[9] This process is accompanied by the release of immunosuppressive factors that dampen adaptive immunity.[10] Efferocytosis in the TME is largely carried out by tumor-associated macrophages (TAMs), one of the most abundant professional phagocytes in the TME.[11] TAMs primarily use MerTK to bring about efferocytosis. MerTK binds to phosphatidylserine on the surface of apoptotic cells through bridging molecules (protein S, growth arrest factor 6) and facilitates apoptotic cell engulfment.[12] Following efferocytosis, TAMs shift towards an anti-inflammatory phenotype associated with the release of immunosuppressive cytokines such as IL-10 and TGF-β and the recruitment of other inflammation-resolving immune cells such as regulatory T cells into the TME.[13] These events make the TME more favorable for tumor growth. Moreover, the M2-like TAMs also facilitate angiogenesis, providing tumors access to nutrients and oxygen and enabling their metastasis.[14]

MerTK activity has been shown to correlate with tumor progression and chemoresistance, and the inhibition of MerTK shows tremendous promise as an anti-cancer therapy.[15] However, most of these therapies involve administering small molecule drugs that cannot be taken up by TAMs preferentially.[16–18] This lack of selectivity can result in adverse side effects that undermine the potential therapeutic benefits of these medications.[19] Delivery vehicles that favor internalization by TAMs are, therefore, desirable in order to improve the therapeutic window of anti-efferocytic therapies.

One strategy for preferential drug delivery to TAMs is to use vehicles with a strong affinity for receptors overexpressed on the TAM cell membrane.[20,21] A prominent feature of the M2-like TAMs is the overexpression of the mannose receptor CD206.[22] This receptor has multiple C-type lectin domains (CTLD) with two of them (CTLD 4 and 5) capable of binding monosaccharides such as mannose, N-acetylglucosamine, and glucose in a Ca^{2+}-dependent manner.[23] Mannose, in particular, has a strong affinity for this receptor, and a vast body of work has been dedicated to demonstrating the feasibility of targeting M2-like macrophages with mannose-decorated drug delivery vehicles.[21] For instance, Glass et al. developed mannose-decorated polyethylene glycol (PEG)-poly (dimethylaminoethyl methacrylate-co-butyl methacrylate) (pDMAEMA-co-BMA) nanoparticles (NPs) to deliver siRNA targeting the inhibitor of nuclear factor-kappa B alpha (IκBα) to TAMs in a TBR5 murine ovarian cancer model. Biodistribution studies showed that the mannosylated NPs were selectively taken up by macrophages with 89% and 34% of the macrophages in the ascites and tumors, respectively, internalizing the mannose NPs.[24] Similarly, Zhang et al. fabricated PBAE-mRNA complexes surface functionalized with mannose dimers (Di-mannose) to target TAMs in an ID8 murine ovarian cancer model. The mRNAs encoded for interferon regulatory factor 5 (IRF5) (a protein that polarizes macrophages to a cytotoxic M1

phenotype) and IKKβ (a kinase that activates IRF 5). The Di-mannose NPs exhibited a 3-fold and 3.6-fold greater accumulation in macrophages and monocytes, respectively, compared to untargeted NPs. Moreover, analysis of the peritoneum macrophage phenotype showed a decrease in the percentage of immunosuppressive macrophages and an increase in the percentage of inflammatory macrophages with corresponding increases in inflammatory cytokines.[25]

Studies featuring mannosylated NPs to deliver therapies preferentially to TAMs typically feature mannose monomers capable of only weak interactions with the mannose receptor compared to polymeric forms of mannose.[26,27] The increased affinity of polymeric mannose with the mannose receptor is due to the simultaneous binding of multiple covalently-linked mannose molecules, resulting in avidity that fosters improved endocytosis by TAMs.[27] Polymeric mannose has been used to target macrophages *in vivo* in tissues outside of tumors.[28,29] However, there persists a significant gap in research on the use of polymeric mannose nanoparticles to target drugs to TAMs.

Here, we report the development of polymeric mannose NPs (PMAM NPs) capable of preferentially delivering UNC2025 (MerTK inhibitor) to TAMs, leading to improved antitumor immunity in a murine breast cancer model **(Figure 1)**. The PMAM NPs are made from a diblock copolymer comprising poly[2-(diisopropylamino)ethyl methacrylate]-*b*-poly(methacrylamido mannose) (PDPA-*b*-PMAM). PDPA, a hydrophobic pH-responsive polymer, formed the core of the NPs and facilitated the loading of lipophilic small molecule drugs and their subsequent release at endosomal pH. PMAM enabled NP stability and preferential uptake by TAMs. Internalization of the PMAM NPs was compared to polyethylene glycol methyl ether methacrylate (PEGMA) NPs with similar physicochemical properties. Lastly, we demonstrate the potential of PMAM NPs

for *in vivo* delivery and show that UNC2025-loaded PMAM NPs achieve antitumor immunity in a triple-negative breast cancer (TNBC) model.

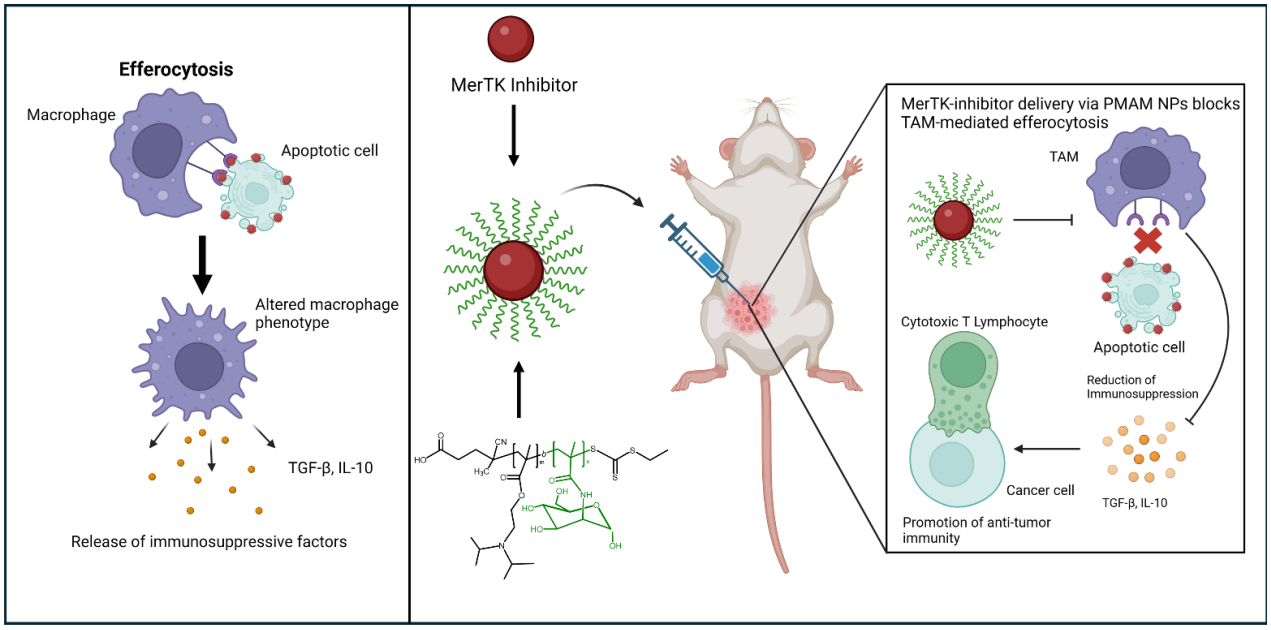

Figure 1. Efferocytosis in the TME polarizes TAMs into an anti-inflammatory phenotype and is accompanied by the release of immunosuppressive factors into the TME. These immunosuppressive factors hinder antitumor immunity. Blocking efferocytosis by delivering a MerTK inhibitor through our PDPA-*b*-PMAM NPs reduces immunosuppression in the TME and promotes antitumor immunity. Created in https://BioRender.com.

2. Results and Discussion

2.1 Synthesis of PDPA-*b*-PEGMA and PDPA-*b*-PMAM diblock copolymers

PDPA diblock copolymers with second blocks comprising either PMAM (PDPA-*b*-PMAM) or PEGMA (PDPA-*b*-PEGMA) were synthesized using RAFT polymerization. To develop these copolymers, we first synthesized a PDPA homopolymer using 4-cyano-4-{[(ethylsulfanyl)carbonothioyl]sulfanyl}pentanoic acid (ECT) as a chain transfer agent (CTA) and confirmed synthesis by identifying the backbone proton peaks at 1.0 ppm (methyl group) and 1.82 ppm (methylene group) and pendant group proton peaks at 2.63 ppm (O-linked methylene group), 2.99 ppm (isopropyl group) and 3.84 ppm (N-linked methylene group) in the ^{1}H-NMR spectrum.

We then synthesized a polymerizable methacrylamidomannose (MAM) monomer by reacting D-mannosamine HCl with methacryloyl chloride. The successful synthesis of MAM was confirmed by the identification of methacrylate protons at 5.15-5.60 ppm in the ^{1}H-NMR spectrum **(Figure S1)**. PDPA-ECT was then chain extended with MAM or PEGMA to form diblock copolymers **(Figure S2)**. The successful synthesis of the diblock copolymers was confirmed by a reduction in the elution time between the diblock copolymers and the PDPA homopolymer in the gel permeation chromatography (GPC) traces. The MWs of PDPA, PDPA-*b*-PMAM, and PDPA-*b*-PEGMA were 26.2kDa (PDI: 1.09), 39.1kDa (PDI: 1.05), and 55.9kDa (PDI: 1.07) respectively **(Table 1).** Further confirmation was achieved by identifying the protons of the mannose ring (3.55-4.42ppm) for PDPA-*b*-PMAM or methylene proton (3.64 ppm) for PDPA-*b*-PEGMA pendant group in the ^{1}H-NMR spectrum **(Figure S3)** and the presence of an -OH peak in the FTIR spectrum between 3200 to 3500 cm^{-1} (PDPA-*b*-PMAM) **(Figure S4).**

2.2 Physicochemical Characterization of PEGMA and PMAM NPs

NPs were made from the PDPA-*b*-PMAM and PDPA-*b*-PEGMA diblock copolymers by dissolving the polymers in dimethyl sulfoxide (DMSO) and tetrahydrofuran (THF), respectively, and then dialyzing against water. PDPA-*b*-PMAM and PDPA-*b*-PEGMA NPs had sizes of approximately 130 nm and 110 nm, respectively, with neutral-to-negative surface charges of -1.355 ± 4.86 and -3.471 ± 0.5123, respectively **(Table 1)**. TEM micrographs corroborated the sizes obtained by DLS and showed that both NPs had a spherical morphology **(Figure 2A-B)**. The cytocompatibility of the NPs was determined by observing the viability of RAW 264.7 macrophages and 4T1 breast cancer cells for 24 h after incubation with increasing concentrations of the NPs. For both NPs at all concentrations, the viability of both the macrophages and the 4T1 cells was greater than 75%, confirming that all NPs were cytocompatible **(Figure 2C-D)**. The

structural stability of the NPs in serum was then assessed by incubating the NPs with FBS at varying concentrations (0-40%) for six hours and monitoring the FRET pair DiO/DiI over time. The FRET efficiency remained steady for the duration of the experiment, indicating a negligible influence of serum proteins on the structural stability of both the PEGMA and PMAM NPs **(Figure 2E)**. The encapsulation and loading efficiency of the PDPA-*b*-PMAM NPs were determined for DiO and UNC2025 (MerTK inhibitor) using fluorescence spectroscopy and UV-VIS, respectively. The standard curves used to obtain the encapsulation efficiency are presented in **Figure S5.** For DiO, the PDPA-*b*-PMAM NPs had an encapsulation and loading efficiency of 80 ± 8.7% and 3.03 ± 0.3%, respectively, while encapsulation and loading efficiencies of 40 ± 1.1% and 1.52 ± 0.04%, respectively, were obtained for UNC2025 (**Table 1).** The difference in encapsulation efficiency between the NPs can be ascribed to the different fabrication processes used to produce NPs with similar physicochemical properties. PMAM NPs are prepared in DMSO in which UNC2025 is highly soluble, whereas PEGMA NPs must be prepared in THF. Both are dialyzed against water to achieve nanoparticle formation. However, the difference in starting solvent causes variation in the final encapsulation efficiency.

Polymer	**PDPA**	**PDPA-*b*-PEGMA (PEGMA NPs)**	**PDPA-*b*-PMAM (PMAM NPs)**
Molecular Weight (kDa)	26.2	55.9	39.1
Polydispersity	1.09	1.07	1.05
Size (nm)	-	110±2.4	137±7.4
Zeta Potential		-3.471±0.5	-1.355±4.9
Encapsulation Efficiency (%)	-	15±0.6	80 ± 8.7%
Loading Efficiency (%)	-	0.6±0.02	3.0 ± 0.3%

Table 1: Polymer and NP physicochemical properties

2.3 pH-dependent drug release via the pH-responsive polarity of PDPA

The relatively acidic pH of the endosome compared to physiological pH provides an avenue for spatiotemporal drug release by NPs whose integrity is compromised at pHs below physiological pH. NPs with a core made of PDPA, a hydrophobic polymer with a pKa of about 6.3, can take advantage of this pH discrepancy for drug delivery. At pHs around 6.3 and below, PDPA becomes protonated and transitions from hydrophobic to hydrophilic, causing the disassembly of PDPA-based NPs.[30] To probe the ability of the NPs to release cargo in a pH-dependent manner, the NPs were prepared with the hydrophobic dye Nile Red and were treated with phosphate buffers with pH ranging from 7.4 to 5.0. At pH 7.4, the NPs remained relatively intact, displaying a negligible loss in fluorescence with time for the duration of the experiment (**Figure 2F**). However, a sudden drop of fluorescence is observed at pHs below the pKa of PDPA (pH 6.0 and 5.0), indicating an instantaneous burst release of the encapsulated dye at endo/lysosomal pHs. Moreover, an inverse relationship between the degree of fluorescence lost and the pH is observed, with lower pHs having a greater amount of release, further highlighting the pH-dependency of cargo release (**Figure 2F**). We further confirmed that UNC2025 followed a similar release pattern, where minimal release of the compound occurred at pH 7.4 while rapid release was triggered at acidic pH's representing the endolysosomal pathway (**Figure S6**).

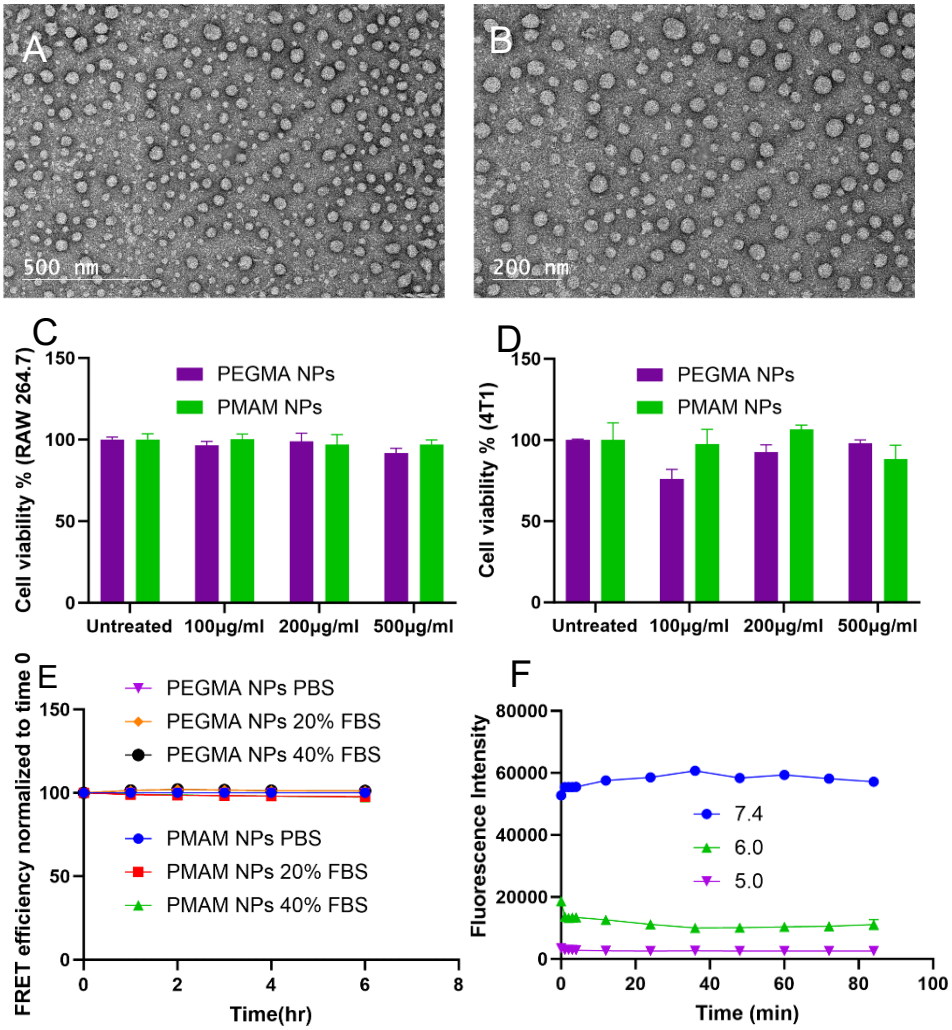

Figure 2: Physicochemical and *in vitro* biocompatibility characterization of PEGMA and PMAM NPs.
TEM images of PMAM NPs (A) at 500 nm scale bar and (B) at 200 nm scale bar Cell viability of (C) RAW 264.7 macrophages and (D) 4T1 breast cancer cells after incubating with varying concentrations of PMAM and PEGMA NPs for 24 h. The data presented are mean values ± standard error of the mean (SEM) (E) Nanoparticle stability over time in different serum concentrations was determined for PMAM and PEGMA NPs using a FRET reporter assay. (F) pH-dependent cargo release of PMAM NPs after incubation in varying pH from 5.0 to 7.4.

2.4 Preferential internalization of PMAM NPs in macrophage cell cultures

The overexpression of the macrophage mannose receptor (MMR; CD206) is a hallmark of TAMs, and mannose is one of the most prominent carbohydrate ligands for this receptor.[31] We designed PMAM NPs to maximize the affinity between MMR and our NPs via multivalent binding

by polymeric mannose ligands since MMR contains eight total carbohydrate recognition domains (CRDs). We first assessed whether PMAM NPs could facilitate greater internalization in macrophages than PEGMA NPs by performing uptake studies *in vitro* using RAW 264.7 macrophages. Incubation was done for two hours, after which the PMAM NPs showed a 12-fold increase in internalization compared to the PEGMA NPs **(Figure 3A)**. After establishing the superior internalization of the PMAM NPs compared to the PEGMA NPs in macrophages, we wanted to confirm that the enhanced uptake was MMR-dependent. To verify the role of MMR in PMAM NP uptake, blocking experiments were conducted by pretreating macrophages with 12.5 mM of D-mannose to inhibit the mannose receptor before NP incubation. Pretreating the macrophages caused a significant decrease in the uptake of the PMAM NPs, while D-mannose pretreatment had no impact on the uptake of the PEGMA NPs **(Figure 3B)**. The superior uptake of the PMAM NPs in macrophages compared to the PEGMA NPs aligns with previous studies contrasting the internalization of mannosylated and PEGylated NPs. For instance, Zhu et al. reported a 75% reduction in macrophage internalization of PEGylated NPs compared to mannosylated NPs.[26] Also, Lopukhov et al. showed a 500% increase in transfection of IC-21 macrophages after modifying PEG-poly(γ(N-[N-(2- aminoethyl)-2-aminoethyl] aspartamide) (PEG-*b*-p(Asp(DET))) with mannose.[32] Importantly, our approach enables the controlled synthesis of PMAM polymeric mannose ligands, which could greatly improve TAM specificity compared to prior technologies based on monomeric mannose-targeting ligands.

We further sought to confirm the specificity of the PMAM NPs by assessing internalization in 4T1 murine breast tumor cells, which do not express high levels of MMR. Contrary to the macrophage uptake studies, however, the PEGMA NPs showed a 1.5-fold greater internalization than the PMAM NPs in the 4T1 breast cancer cells, further highlighting the preferential nature of

PMAM NP uptake in macrophages as opposed to other cell types that will be prominent in the TME **(Figure 3C)**. While not tested directly in the current report, we hypothesize that reduced protein adsorption on the PMAM NP surfaces leads to reduced cell interaction and uptake in the 4T1 cell line. *In vitro* macrophage uptake of DiO-loaded PMAM and PEGMA NPs with or without pretreatment with D-mannose was also assessed through fluorescence microscopy. As can be seen from **Figure 3D,** the treatment group "**PMAM NPs/No D-mannose**" which represents macrophages incubated with PMAM NP and without D-mannose pretreatment, had the highest NP internalization and more widely distributed DiO fluorescence. Pretreating the macrophages with D-mannose before PMAM NP incubation (**PMAM NPs/D-mannose**) significantly reduced NP uptake, as shown by lower DiO fluorescence and less cellular distribution of the NPs. The internalization of PEGMA NPs was markedly lower than the internalization of the PMAM NPs for both untreated and D-mannose-treated groups. Moreover, D-mannose pretreatment did not affect PEGMA NP internalization. Altogether, the fluorescence microscopy images corroborate the flow cytometry results, further confirming the PMAM NPs' superiority in targeting macrophages compared to PEGMA NPs.

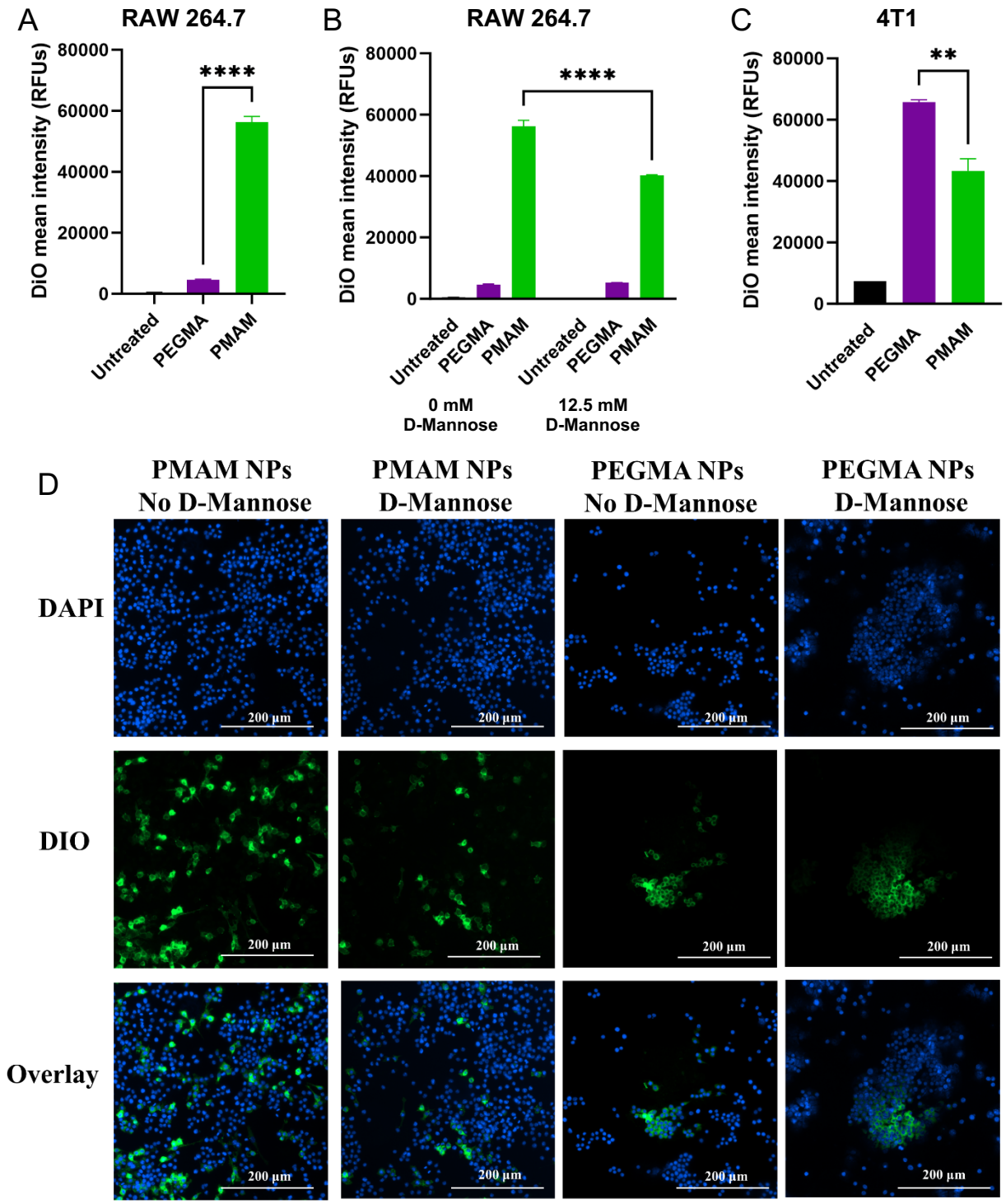

Figure 3: Preferential macrophage internalization by PMAM NPs is MMR-dependent.

(A) Internalization of PMAM and PEGMA NPs in RAW 264.7 macrophages after 2 h. (n=3, ****p< 0.0001 (Tukey's test)) (B) Macrophage internalization of PMAM and PEGMA NPs after pretreatment with 12.5 mM D-mannose. (n=3, ****p< 0.0001 (Tukey's test)) (C) PMAM and

PEGMA NP internalization in 4T1 breast cancer cells. (n=3, **p< 0.001 (Tukey's test)) (D) Confocal microscopy images of RAW 264.7 macrophages treated with PMAG (without D-mannose pretreatment, first column; with D-mannose pretreatment, second column) and PEGMA NPs (without D-mannose pretreatment, third column; with D-mannose pretreatment, fourth column). The data presented are mean values ± SEM. The p values displayed represent PMAM NPs vs PEGMA NPs.

2.5 Tumor retention and preferential TAM uptake of PMAM NPs *in vivo*

Following the successful *in vitro* internalization studies in which the PMAM NPs showed significantly greater uptake in macrophages compared to PEGMA NPs, as well as corroboratory results from similar studies discussed above, we decided to move forward with the PMAM NPs for further evaluation *in vivo*. We assessed biodistribution and preferential internalization by macrophages *in vivo* in the 4T1 murine breast cancer model. Tumor-bearing mice were intratumorally injected with PMAM NPs, after which tumor and major organs were harvested 24 h post-injection and imaged on an IVIS. As can be seen in **Figures 4A**-**B**, the PMAM NPs remain largely localized to the tumor with minor accumulation in the liver. The tumors were then processed to make single-cell suspensions to determine the distribution of PMAM NPs among the cell populations of the TME. We specifically looked at NP accumulation in TAMs (F4/80+) compared to tumor cells (EpCAM+). Although control PEGMA NPs show similar tumor retention to PMAM NPs after intratumoral injection, PEGMA NPs show no significant difference between accumulation in tumor cells (EpCAM+) and macrophages (F4/80+) *in vivo* (**Figure 4C**). However, there was an approximately 33% increase in the internalization of PMAM NPs by TAMs compared to tumor cells in the TME **(Figure 4D-E)**. This increase in uptake indicates that PMAM NPs preferentially accumulate in TAMs as opposed to tumor cells *in vivo*, though albeit, we did observe substantial tumor cell accumulation as well. This is likely due to the intratumoral administration route delivering a very large bolus dose of NPs into the TME, some of which were able to

accumulate off-target in tumor cells as opposed to TAMs. However, we do not expect substantial negative consequences of tumor cell accumulation in this setting since the off-target side effects of efferocytosis-targeted therapies is primarily due to the inhibition of efferocytosis in systemic monocytes.

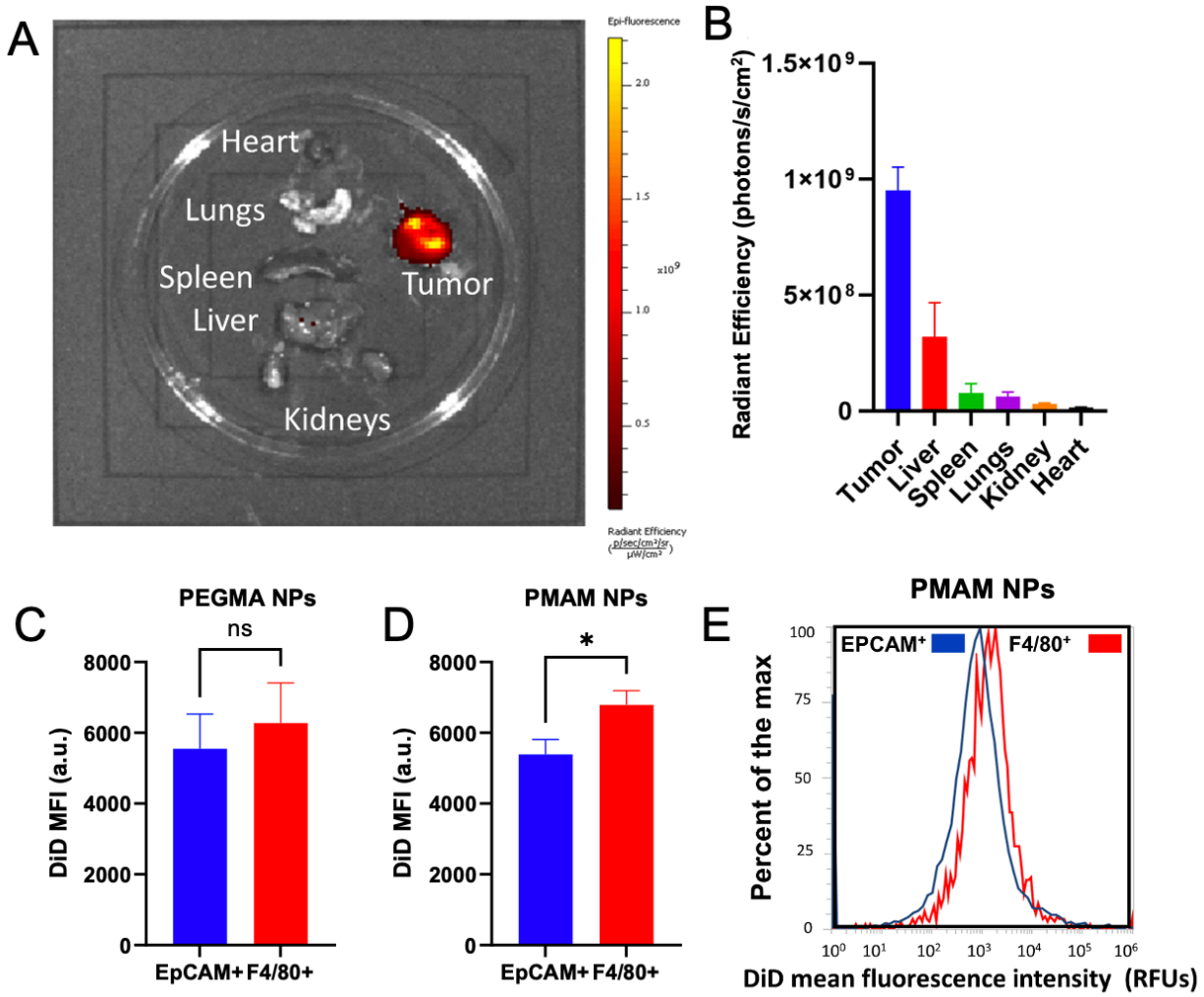

Figure 4: Tumor retention and preferential TAM uptake of PMAM NPs *in vivo*
(A) Representative IVIS image showing biodistribution of PMAM NPs after intratumoral administration (B) Mean DiD fluorescence intensities of the tumor and major organs after intratumoral administration of PMAM NPs. Mean DiD fluorescence intensities of tumor cells (EPCAM+) and TAMs (F4/80+) after intratumoral administration of PEGMA (C) and (D) PMAM NPs (n=5, *p<0.05). The data presented are the mean values ± SEM. (E) Representative fluorescence histogram of tumor cells (EPCAM+) and TAMs (F4/80+) from PMAM NP-treated mice.

2.6 Therapeutic efficacy and biocompatibility of UNC2025-loaded PMAM NPs in 4T1 breast cancer xenografts

After confirming that the PMAM NPs are preferentially internalized by TAMs in the TME, we sought to assess the effects of blocking TAM-mediated efferocytosis on antitumor immunity. We again established 4T1 tumors in BALB/c mice and began treatment once the tumors reached 100 mm^3. The mice were administered either UNC2025-loaded PMAM NPs, free UNC2025, or saline once a week for three weeks (**Figure 5A**). Both free UNC2025 and UNC2025-loaded PMAM NPs significantly inhibited tumor growth compared to control. Interestingly, the UNC2025-loaded PMAM NPs significantly inhibited tumor growth compared to free UNC2025, highlighting the enhancement of tumor efficacy of UNC2025 due to PMAM NP-mediated delivery (**Figure 5B**). The group treated with saline saw a rapid, sustained increase in tumor volume, resulting in a final tumor volume of 1700 ± 129.1 mm^3. Treatment with free UNC2025 mildly delayed the rise in tumor volume until day 15, when tumor volume began to rise at a rate similar to control. The UNC2025-loaded PMAM NP treatment group had a slower increase in tumor volume compared to the other groups after the first week, and the rate of proliferation seemed to decrease towards the endpoint of the experiment, indicating an increase in antitumor efficacy with repeated administration of drug-loaded NPs. The enhanced antitumor efficacy of UNC2025-loaded PMAM NP treatment resulted in a final volume of 800 ± 129.8 mm^3, less than half the size of saline-treated controls. Slight increases in body weight were observed for each treatment group (**Figure 5C**). Importantly, UNC2025-loaded PMAM NPs did not negatively impact body mass, even with repeated treatment. Analysis of tumor weights showed the same trend as the tumor volume, with the saline-treated group having the largest average tumor weight of 2.71 ± 0.085 g at the endpoint **(Figure 5E)**. UNC2025 treated animals had an average tumor weight of 2.20 ±

0.112 g, which was not significantly less than the control group. However, UNC2025-loaded PMAM NP-treated animals had an average tumor weight of 1.85 ± 0.098 g, or about a 32% ($p=0.012$) reduction in average tumor weight compared to saline-treated animals. Histological analysis of tumor sections obtained from each treatment group revealed the infiltration of mononuclear immune cells, such as lymphocytes, into the tumor with the UNC2025-loaded PMAM NP-treated animals showing significant infiltration of immune cells **(Figure 5F)**. Moreover, the tumors of animals treated with UNC2025-loaded PMAM NPs showed much lower density of tumor cells compared to other treatment groups. In sum, these results indicate that TAM-targeted PMAM NPs harboring the MerTK inhibitor UNC2025 efficiently block breast cancer growth via efferocytosis blockade in the TME.

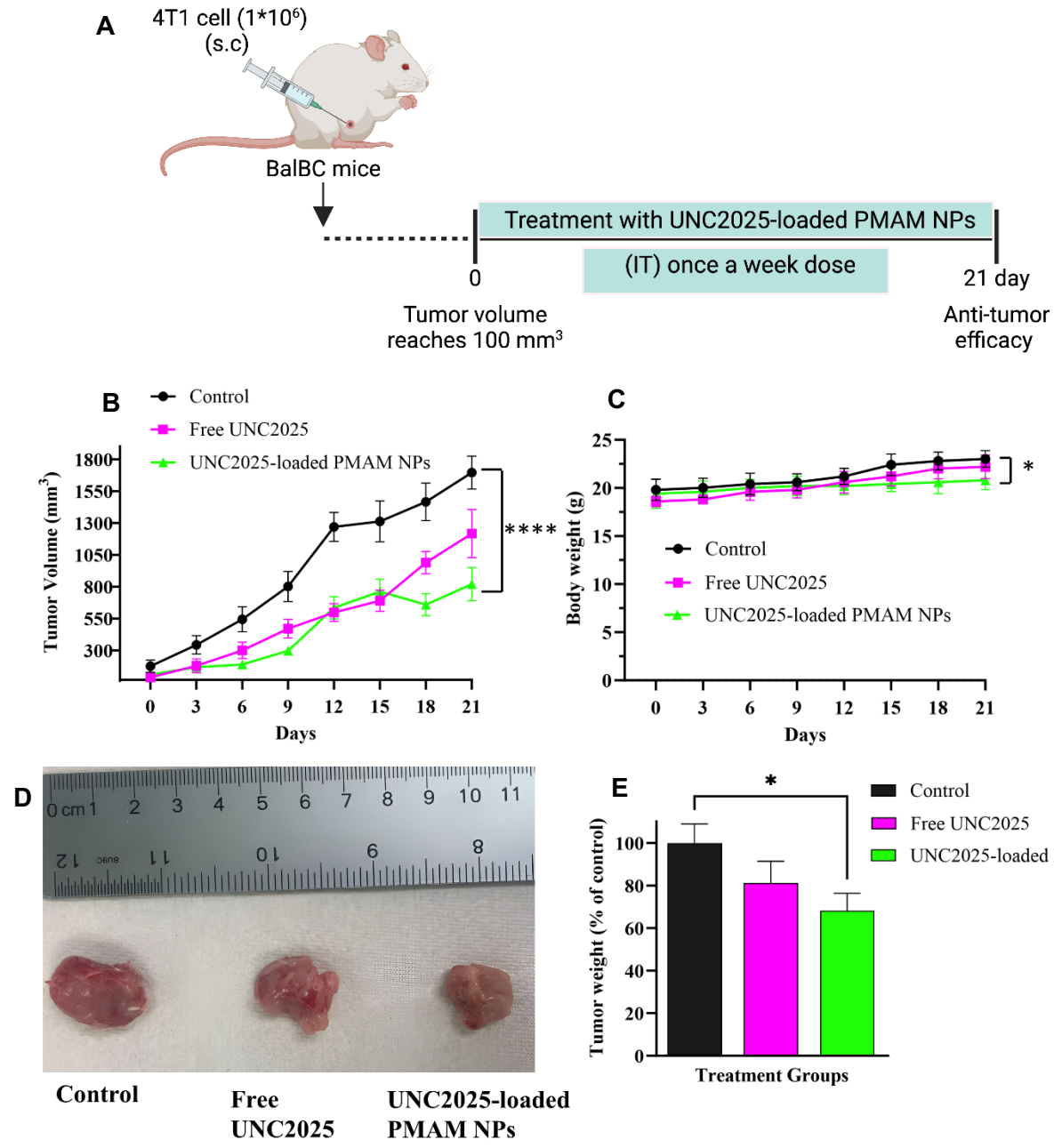
A
4T1 cell (1*10⁶)
(s.c)
BalBC mice
Treatment with UNC2025-loaded PMAM NPs
(IT) once a week dose
0
21 day
Tumor volume
reaches 100 mm³
Anti-tumor
efficacy
B
Control
Free UNC2025
UNC2025-loaded PMAM NPs
Tumor Volume (mm³)
1800
1550
1300
1050
800
550
300
****
0 3 6 9 12 15 18 21
Days
C
Body weight (g)
25
20
15
10
5
0
*
Control
Free UNC2025
UNC2025-loaded PMAM NPs
0 3 6 9 12 15 18 21
Days
D
0 cm 1 2 3 4 5 6 7 8 9 10 11
Control
Free
UNC2025
UNC2025-loaded
PMAM NPs
E
*
Control
Free UNC2025
UNC2025-loaded PMAM NPs
Tumor weight (% of control)
100
80
60
40
20
0
Treatment Groups
F
Control
UNC2025
UNC2025-loaded PMAM NPs
100μm
100μm
100μm

Figure 5: Therapeutic efficacy of UNC2025-loaded PMAM NPs in 4T1 breast cancer xenografts.
(A) Timeline depicting induction of 4T1 breast tumors and treatment regimen. Created in https://BioRender.com. (B) Change in tumor volume over time after treatment with UNC2025-loaded PMAM NPs or free UNC2025 (n=5, ****p< 0.0001 (Tukey's test)). (C) Change in body weight over time after treatment with UNC2025-loaded PMAM NPs or free UNC2025 (n=5, *p<0.05 (Tukey's test)). (D) Representative image showing tumor sizes at endpoint for control, free UNC2025, and UNC2025-loaded PMAM NPs. (E) Mean tumor weights at the endpoint after treatment with UNC2025-loaded PMAM NPs or free UNC2025 (n=5, *p < 0.05 (Tukey's test)). (F) Hematoxylin and Eosin-stained section of control (left), free UNC2025 (middle), and UNC2025-loaded PMAM NPs (right) at 40X magnification. White arrows point to mononuclear immune cell infiltrates. The data presented are the mean values ± standard deviation (SD). The p values reported are of UNC2025-loaded PMAM NPs vs control.

We also assessed the biocompatibility of the UNC2025-loaded PMAM NP by evaluating biochemical hematological profiles at the conclusion of treatment. For the liver, the serum biochemistry marker alanine aminotransferase (ALT) falls within the normal range (111 ± 104 to 239 ± 141) for all treatment groups. Aspartate aminotransferase (AST) concentrations were higher than the normal range (126.95-156.70) in all treatment groups, with the UNC2025-loaded PMAM NPs group having concentrations closest to the normal range.[33–35] This indicates that the increase in AST concentration was likely due to tumor burden and that treatment with UNC2025-loaded PMAM NPs attenuated the adverse effects of the disease. For the kidney, no sign of toxicity was observed from the serum chemistry as the blood urea nitrogen (BUN) fell within the normal range for all treatments.[36] **(Figure 6A-C) (Table S1)**. Moreover, the hematological parameters fell within the normal physiological range [Red Blood Cells (RBC, 7.48-10.52); Hemoglobin (HGB, 11.15-16.12)] except for the white blood cells (WBC), which shows elevated concentrations across all treatment groups, suggesting increased immune activity due to tumor burden.[33,35,37] **(Figure 6D-F) (Table S2)**. Similar to the biochemical markers of liver and kidney function (AST, ALT,

and BUN), UNC2025-loaded PMAM NPs decreased WBC counts, again supporting the notion that the UNC2025-loaded PMAM NPs decreased tumor burden significantly compared to controls.

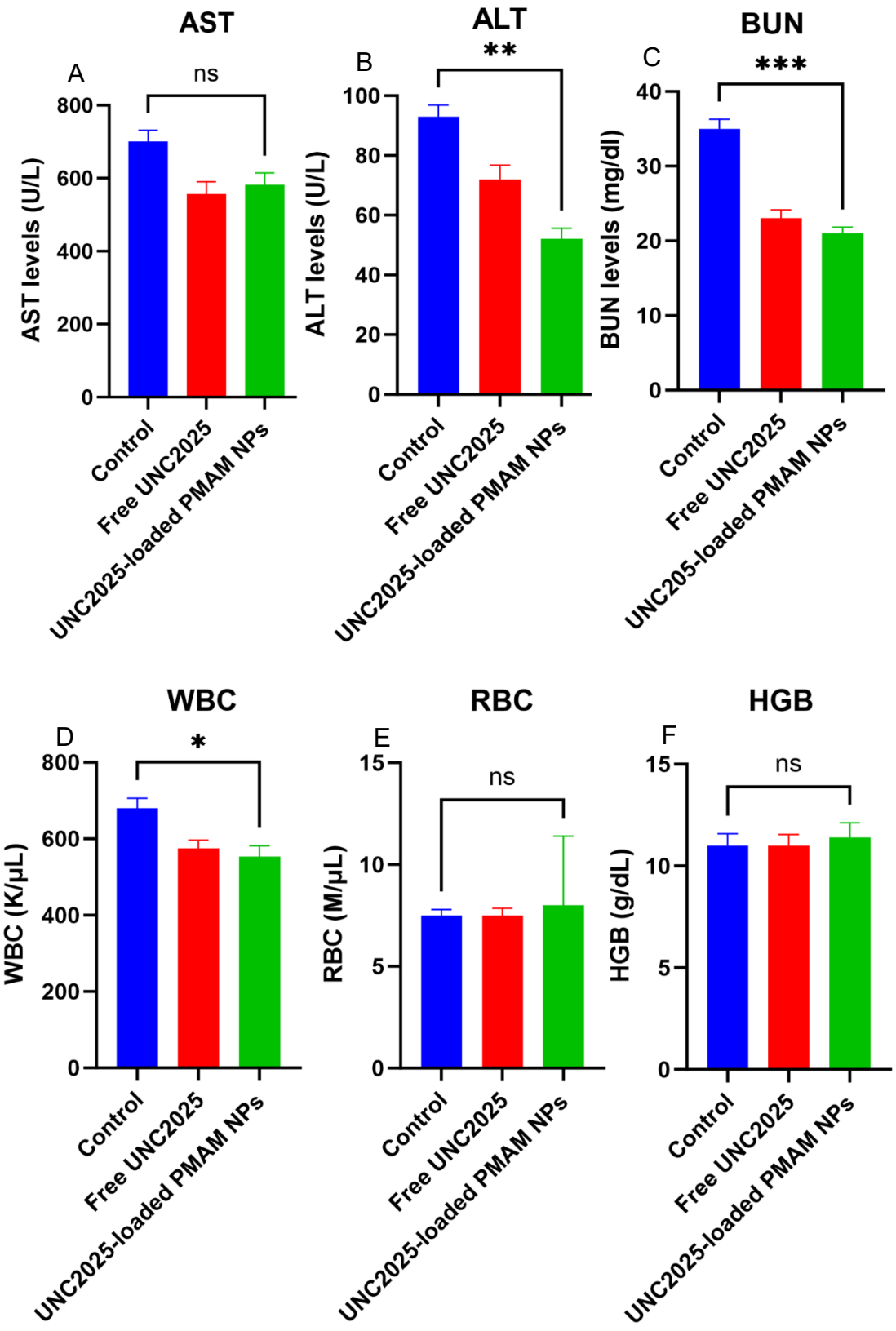

Figure 6: Biocompatibility studies of UNC2025 loaded-PMAM NPs after intratumoral administration

The serum concentrations of markers of liver function (A) ALT (n= 5, **p <0.01(Tukey's test)), (B) AST (n= 5, ns p > 0.05 (Tukey's test)), and kidney function (C) BUN (n= 5, ***p < 0.001(Tukey's test)) after administration of saline, UNC2025, or UNC2025 loaded-PMAM NPs. Counts of (D) WBCs (n= 5, *p< 0.05 (Tukey's test)), (E) RBCs (n= 5, ns p > 0.05 (Tukey's test)), and (F) HGB (n= 5, ns p >0.05 (Tukey's test)) after administration of saline, UNC2025, or UNC2025 loaded-PMAM NPs. The data presented are the mean values ± SEM. The p values displayed represent UNC2025-loaded PMAM NPs vs control.

Modulation of TAM activity is an increasingly appreciated therapeutic approach to promote antitumor immunity against many cancers.[20,38] As one of the most prolific immune cells in the TME, TAMs wield a great influence over the composition of the TME and the adaptive immune response to cancer.[11,39] TAMs predominantly express an anti-inflammatory phenotype, largely due to their role in mediating the efferocytosis of accumulating apoptotic cells in the TME.[10] This phenotype is associated with neoangiogenesis, tumor growth, invasion, metastasis, and chemoresistance.[40] Inhibiting efferocytosis to repolarize TAMs is, therefore, a viable approach to enhance antitumor immunity.

To assess the therapeutic effects of blocking TAM-mediated efferocytosis, we first rationally designed polymeric nanocarriers capable of enhancing the internalization of lipophilic drugs by TAMs. Our design consideration focused on two important parameters: selective uptake in TAMs and spatiotemporally controlled drug release. A variety of receptors have been harnessed to enable selective uptake by TAMs, such as folate receptor beta, the legumain receptor, the transferrin receptor, and the MMR.[41,42] Among these, MMR is the most commonly chosen candidate for drug delivery to TAMs and has the benefit of being the only one that is not expressed on tumor cells.[20] Moreover, the acidification of the endosome on its way to the lysosome creates

an avenue for nanocarriers with pH-responsibility to have precise control over intracellular drug release.[43]

We, therefore, developed PMAM NPs featuring a polymeric mannose outer surface for preferential endocytosis in TAMs via MMR. The PMAM NPs possessed a PDPA core, enabling encapsulation and controlled drug release in the endosome. The NPs had a size of 130 nm and a neutral surface charge. The PMAM NPs showed excellent stability at physiological pH but disassembled at endosomal pH enabling spatiotemporal control of drug release. Moreover, the NPs showed a preference for uptake by cells with MMR *in vitro*. PMAM NPs had significantly higher uptake in macrophages than PEGMA NPs, and internalization of the PMAM NPs was diminished by pretreating macrophages with D-mannose to block MMR. The uptake of PEGMA NPs, unlike that of the PMAM NPs, was unaffected by D-mannose pretreatment. Furthermore, the PMAM NPs showed poor uptake compared to PEGMA NPs in 4T1 breast cancer cells, which do not express MMR. The superior performance of the PMAM NPs compared to PEGMA NPs *in vitro* indicated that we had developed NPs with tremendous potential for selective drug delivery to TAMs *in vivo*. Furthermore, the PMAM NPs display noteworthy advantages over particular polymeric mannose NP formulations documented in the literature. For instance, Rushworth et al. assessed the internalization of polymers consisting of p(butyl methacrylate-co-methacrylic acid)-*b*-(poly(ethylene glycol) methyl ether methacrylate-co-N-hydroxysuccinimide ester)-*qb*-(mannose methacrylate) copolymers (p(BMA-*co*-MAA-b-NMS-*co*-PEGMA-*qb*-ManMA)) in macrophages isolated from the peritoneal cavity of mice. Although the internalization of the (p(BMA-*co*-MAA-b-NMS-*co*-PEGMA-*qb*-ManMA)) copolymers showed some dependence on the mannose receptor, as evidenced by the reduced uptake after mannose receptor blockade, no increase in internalization was observed compared to non-glycosylated polymers. However, a slight increase

in uptake compared to the non-glycosylated polymers was observed after gating for CD206 in the macrophage population.[44] Also, Yu et al. reported a 3-fold increase in macrophage uptake of their mannose-based polymer nanoparticles {poly [(butyl methacrylate-co-2-propyl acrylic acid-co-dimethylaminoethyl methacrylate)-*b*-(dimethylaminoethyl methacrylate)-*b*-(mannose methacrylate)]; poly(BMA-co-PAA-co-DMAEMA)-b-(DMAEMA)-b-(ManMA)}compared to control NPs after four hours which was significantly lower than the increase we observed after just two hours of incubation.[45] While different incubation conditions can account for some of the discrepancies in results, the superior performance highlights the potential of our NP design to enhance therapeutic outcomes beyond those achieved by previous NP designs.

Moving forward with the PMAM NPs, we assessed internalization in TAMs *in vivo* after intratumoral administration. This route of administration has been preferred to intravenous or intraperitoneal administrations in many studies focusing on solid tumors[46–48] due to the possibility of attaining high NP concentration in the TME, the attenuated susceptibility to interstitial barriers, and the reduction of off-target toxicities.[49] In breast cancer specifically, intratumoral administration of therapy-bearing NP has been shown to improve therapeutic outcomes compared to similar administration of free drugs.[50] Moreover, Zhang et al. showed that intratumoral administration of anti-CD44 antibody-polymersome-DM1 conjugates in an MDA-MB-231 murine tumor model led to complete tumor eradication in 80% of mice, whereas intravenous administration only suppressed tumor growth.[51] Furthermore, the intratumoral administration of immunotherapy-bearing NPs also has the potential to generate robust systemic antitumor immunity via the abscopal effect. This effect is a phenomenon in which localized treatment of primary tumors stimulates immunity against metastasized tumors.[52] Cheng et al. demonstrated this effect through the intratumoral delivery of an NP-in-hydrogel (NPH) containing αPD-L1, αCTLA-4, and a

nanovaccine comprising of Toll-like receptor (TLR 7/8/9), and stimulator of interferon genes (STING) in a murine glioblastoma tumor model which featured a subcutaneous primary tumor in the right flank and a distant orthotopic tumor.[53] They showed complete tumor regression of all the primary tumors and, interestingly, complete regression of two-thirds of distant tumors after a single injection of NPH. Buss et al. intratumorally administered tandem peptide nanocomplexes containing a TLR9 ligand to enhance the abscopal effect of intraperitoneally administered αCTLA-4 in mice bearing subcutaneous B16F10 melanoma tumors on both left and right flanks. They found a 50% tumor suppression in the distant tumor compared to αCTLA-4 treatment alone.[54]

The successful uptake of the PMAM NPs by TAMs further confirmed the suitability of the PMAM NPs as a drug delivery platform for TAMs. Next, we intratumorally administered PMAM NPs loaded with the commercially available MerTK inhibitor UNC2025 and compared to the free drug form of UNC2025. We determined antitumor efficacy by monitoring changes in tumor volume for the duration of the experiment and measuring the weight of the harvested tumors at the end of the experiment. The significant reduction in tumor volume and the lower endpoint tumor weight of the group treated with the UNC2025-loaded PMAM NPs compared to free UNC2025 demonstrate the therapeutic benefit of using the PMAM NPs to enable preferential delivery to TAMs. Our results support a growing body of work highlighting the potency of blocking efferocytosis as a therapeutic strategy to promote antitumor immunity. Prominent examples of other NP designs to deliver efferocytosis-inhibiting molecules in the literature are PLGA-PEG NPs[55] and mesoporous silica NPs.[56] The PMAM NPs could hold particular promise compared to these non-targeted NPs because of the preferential TAM uptake of PMAM NPs. Moreover, multiple studies have demonstrated some therapeutic benefits of free UNC2025 in other cancer models apart from breast cancer.[10,57] The superior antitumor efficacy of the UNC2025-loaded

PMAM NPs compared to free UNC2025 suggests that our PMAM NPs could further enhance treatment outcomes in these diseases.

This preliminary study is a proof-of-concept of the suitability of synthetic glycopolymers to enhance drug delivery to TAMs. The convenient location of the tumor allowed for the possibility of intratumoral administration. However, not all cancers are accessible by intratumoral injections and require other forms of delivery, such as intraperitoneal or intravenous administration.[58] The PMAM NPs developed in this work possess suitable physicochemical properties such as 100-200 nm diameter, neutral surface charge, and serum stability, making them versatile drug delivery vehicles compatible with several routes of administration.[59,60] In future studies, we will further assess the ability of the PMAM NPs to enhance the therapeutic outcomes of anti-efferocytic drugs after systemic administration. Moreover, we will investigate the phenotypic changes in TAMs and assess their effects on immunosuppression in the TME to more fully establish the underlying immunological mechanisms for improved therapeutic outcomes. Lastly, as systemic administration of anti-efferocytic drugs increases the chances of autoimmunity, it is interesting to speculate that TAM-targeting PMAM NPs could significantly mitigate the autoimmune side effects of systemic efferocytosis inhibition.

3. Conclusion

Shaping the TME into a more conducive environment for antitumor immunity is an increasingly popular strategy for cancer treatment. Due to the highly involved role of TAMs in tumorigenesis and metastasis, TAM-targeting therapeutics are seen as a promising alternative approach in cancers refractory to traditional immune checkpoint inhibitors. The inability of these therapies to selectively accumulate in TAMs necessitates the use of drug delivery vehicles to improve treatment outcomes. We developed a drug delivery platform capable of enhancing the

efficacy of small molecule, TAM-targeting, anti-cancer therapeutics. The PMAM NPs used the strong avidity between polymeric mannose and the overexpressed mannose receptor on the surface of TAMs to drive preferential delivery. Moreover, the incorporation of a pH-responsive core equipped the delivery platform with the capacity for rapid intracellular drug release. The PMAM NPs show an affinity for macrophages as opposed to tumor cells *in vitro*. Additionally, the PMAM NPs enhanced the blockade of TAM-mediated efferocytosis, leading to improved antitumor immunity in breast cancer. In summary, we show that the targeted blockade of TAM-mediated efferocytosis is a promising strategy that could improve therapeutic outcomes in cancers that are refractory to standard immunotherapeutic approaches.

4. Materials and Methods

4.1. Materials

2-(Diisopropylamino)ethyl methacrylate) (DPA), glucosamine hydrochloride, triethylamine, N, N'-dicyclohexylcarbodiimide (DCC), 4-dimethylaminopyridine (DMAP), 2,2-azobis(2-methylpropionitrile) poly (ethylene glycol) methacrylate (PEGMA) were all purchased from Sigma Aldrich. Tetrahydrofuran (THF), dimethylformamide (DMF), dimethylacrylamide (DMAc), and hydrogen peroxide (H_2O_2) were all purchased from Fisher Chemicals. Dulbecco's modified Eagle's medium, Benzoxazolium, 3-octadecyl-2-[3-(3-octadecyl-2(3H)-benzoxazolylidene)-1-propenyl]-, perchlorate (DiO), 1,1'-Dioctadecyl-3,3,3',3'-Tetramethylindocarbocyanine Perchlorate (Dil), 1,1'-Dioctadecyl-3,3,3',3'-Tetramethylindodicarbocyanine, 4-Chlorobenzenesulfonate Salt (DiD) were purchased from ThermoFisher Scientific.

4.2. Synthesis of Poly(2-(Diisopropylamino)ethyl methacrylate))

Poly(2-(Diisopropylamino) ethyl methacrylate)) (PDPA) was synthesized through the reversible addition-fragmentation chain transfer (RAFT) polymerization of DPA as described in Hu et al.[61] Briefly, DPA (47.7g, 222.9 mmol), ECT (0.315g, 1.486mmol), AIBN (0.0496g, 0.297mmol) were in 99 mL of 1,4-dioxane and added to a 500 mL round-bottom flask. Nitrogen was bubbled for 30 min, after which the polymerization was carried out at 70 ^{o}C for 24 h. The product was purified by dialyzing against acetone for 24h. ^{1}H NMR (400 MHz; $CDCl_3$, δ): 1.01 ppm (($CH(CH_3)_2$; CH_3{methacrylic}), 1.72-2.07 ppm (CH_2), 2.64 ppm (CH_2CH_2N), 2.99 ppm ($(CH\text{-}N)_2$), 3.84 ppm (OCH_2CH_2). (PDPA, M_n, = 26,220 g/mol, PDI = 1.09)

4.3. Synthesis of 2-methacrylamide mannose (MAM)

MAM was prepared according to the procedure described in Pearson et al.[62] with some modifications. Briefly, D-Mannosamine HCl (10g, 0.0465 mol), sodium carbonate (7.38g, 0.0696 mol), and sodium nitrite (0.201g, 0.00291mol) were dissolved in 28.8 mL of DI water and placed in an ice/salt bath at -10 ^{o}C. Methacryloyl chloride (4.6 mL, 0.0481 mol) was then added dropwise, and the mixture was stirred for 2 h while maintaining the temperature at -10 ^{o}C. The reaction was then allowed to proceed at RT overnight after which the salts formed as byproducts of the reaction were precipitated in cold methanol. MAM was obtained by adding ethyl acetate at four times the volume of methanol in the mixture. The precipitate was collected by filtration and dried in a vacuum oven. ^{1}H NMR (400 MHz; D_2O) δ (ppm) 1.84 (s, 3H, $C(O)CH_3$), 3.41–3.86 (m, 6H, $H_{2,3,4,5,6,6'}$), 4.03 (d, 1H), 5.15 (d, H, $C{=}CH_2$), 5.45 (s, 1H, $C{=}CH_2$), 5.6 (s, 1H, NH).

4.4. Synthesis of PDPA-b-PMAM

MAM (911 mg, 3.688 mmol), PDPA (728 mg, 0.028mmol), and AIBN (1.15 mg, 0.00684 mmol) were dissolved in 8 mL of DMAc in a 25 mL oval-shaped flask; then the solution was degassed with nitrogen for 30 minutes. The polymerization was performed at 70 °C for 24 h and then purified by dialyzing against methanol for 24 h. ^{1}H NMR (400 MHz; DMF, δ): ^{1}H NMR (400 MHz; DMF, δ): 1.00-1.97 ppm (($CH(CH_3)_2$; CH_3{methacrylic}), 1.98-2.36 ppm (CH_2), 2.94 ppm (CH_2CH_2N), 3.11 ppm ($(CH\text{-}N)_2$), 3.55-4.42 ppm (m, 6H, $H_{2,3,4,5,6,6'}$), 3.84 (OCH_2CH_2) (M_n, = 39,160 g/mol, PDI = 1.047)

4.5. Synthesis of PDPA-b-PEGMA

PDPA-*b*-PEGMA was prepared according to the method described in Hu et al.[61] PEGMA (3 g, 6.06 mmol), PDPA (2396 g, 0.1126 mmol), and AIBN (3.1 mg, 0.01876 mmol) were dissolved in 20 mL of dioxane in a 50 mL round-bottom flask, and then the solution was degassed with nitrogen for 30 minutes. The polymerization was performed at 70 °C for 24 h and then purified by dialyzing against methanol for 24 h. Methanol was then evaporated in a vacuum oven, yielding a white-yellow product. ^{1}H NMR (400 MHz; DMF, δ): ^{1}H NMR (400 MHz; $CDCl_3$, δ): 1.01 ppm (($CH(CH_3)_2$; CH_3{methacrylic}), 1.72-2.07 ppm (CH_2), 2.64 ppm (CH_2CH_2N), 2.99 ppm ($(CH\text{-}N)_2$), 3.64 (M, $-OCH_2\text{-}CH_2$), 3.84 ppm (OCH_2CH_2).

4.6. Polymer characterization

Gel permeation chromatography (GPC) was used to obtain the molecular weights of the polymers. GPC was conducted using Eprogenv b CATSEC 100 and CATSEC 300 columns in series and a mobile phase comprising water with 1% acetic acid and 0.1M Na_2SO_4. Wyatt miniDAWN TREOS light scattering detector and Opti-TrEX refractive index detector (Wyatt

Technology Corp., Santa Barbara, CA, USA) were used to obtain absolute molecular weights. ^{1}H NMR spectra were obtained in chloroform (PDPA) and DMF (PDPA-*b*-PMAM and PDPA-*b*-PEGMA) using a Brüker 400 MHz spectrometer. FTIR spectra were obtained in the attenuated total reflectance (ATR) mode using an Agilent Technologies Carry 600 Series FTIR Spectrometer with a diamond crystal. Experiments were performed at a resolution of 4 cm^{-1} over a spectral range of 4000–400 cm^{-1} with 100 scans.s

4.7. Nanoparticle synthesis and characterization

NPs were formed from the diblock copolymers by dissolving 4 mg of each copolymer in 1 mL of either DMSO (PDPA-*b*-PMAM) or THF (PDPA-*b*-PEGMA) and dialyzing against water for 24 h. The mixture was then dialyzed against water for 24 h and filtered through a 0.2 μm syringe filter. Size and surface charge measurements were obtained by dynamic light scattering (DLS) using a Malvern Zetasizer PRO. The critical micelle concentration (CMC) was obtained by static light scattering (SLS) using an LS Spectrometer by LS Instruments. To determine the encapsulation and loading efficiency of NPs, NPs were prepared using a 1:25 ratio of dye to polymer. The NPs were filtered with a 0.45 μm filter to remove the unencapsulated dye, lyophilized, and redissolved in DMSO. To perform TEM, the NPs were placed onto one copper mesh grid via micropipette for one minute, then blotted with filter paper to remove excess solution. The samples were stained with 2% Uranyl Acetate for 20 seconds, then blotted to remove excess stain. Each grid was dried in a vacuum for 20 minutes. Imaging was performed at 200 kV on a JOEL 2100 TEM. Fluorescence measurements were taken, and the amount of dye encapsulated was obtained using a standard curve. The formulas below were used to calculate the encapsulation and loading efficiencies, respectively.

$$Encapsulation\ efficiency = \frac{\text{Mass of encapsulated dye}}{\text{Mass of dye added}} \times 100 \qquad \textbf{4.1}$$

$$Loading\ efficiency = \frac{Mass\ of\ loaded\ dye}{Mass\ of\ NP + mass\ of\ loaded\ dye} \times 100 \qquad \textbf{4.2}$$

4.8. Serum stability studies

The stability of the nanoparticles in serum was assessed by incubating them with varying concentrations of FBS (0-40%). The nanoparticles were prepared as described in our previous work[63] containing 1 wt% of the FRET pair DiO/DiI. The decrease in FRET intensity with time, which occurs as the nanoparticle disassembles and cargo is released, was measured over 6 h using a microplate reader (BioTeK synergy H1) at an excitation wavelength of 480 nm and emission wavelengths of 530 nm (DiO) and 580 nm (DiI) and the FRET efficiency was obtained.

4.9. pH-triggered in vitro cargo release

pH-dependent cargo release was assessed by treating NPs with different pHs (pH 5.0-7.4) and measuring the release of Nile Red cargo. The nanoparticles were prepared at a concentration of 1mg/mL containing 1% Nile red. 100 µL of the polymer solution was added into each well used in the 96-well plate, followed by treatment with increasing concentrations of (pH 5.0-7.4). The change in fluorescence with time was monitored for a 96 h duration using the BioTeK microplate reader at excitation and emission wavelengths of 545 nm and 612 nm, respectively, and normalized to control.

4.10. Cytocompatibility studies

The cytocompatibility of the NPs was measured by assessing the cell viability of RAW 264.7 murine macrophages and 4T1 breast cancer cells after incubation with increasing

concentrations of the NPs (0-500 μg/mL). The cells were seeded in three replicates in 96-well plates at a density of 10,000 cells/well. The media comprised DMEM with 10% FBS and 1% antibiotic-antimycotic. The cells were allowed to adhere and proliferate for 24 h before replacing the media with new media containing varying concentrations of NPs. The cells were incubated with the new media for 24 h, after which a glow assay (CellTiter Glo^{TM}) was performed, and the luminescence of the cell solutions was measured on the BioTek microplate reader.

4.11. Cellular internalization

Cellular internalization studies were performed in RAW 264.7 macrophages and 4T1 breast cancer cells. The cells were seeded in three replicates at a density of 100,000 cells/well in 12-well plates with media comprised of DMEM with 10% FBS and 1% antibiotic-antimycotic and allowed to adhere for 24 h. PMAM and PEGMA NPs with DiO were prepared at a concentration of 2.5 mg/mL. The NPs were diluted with media to have a final concentration of 250 μg/mL. The cells were incubated with the NP solution in media for 2 h and then prepared for flow cytometry analysis. Flow cytometric analysis was conducted using an Invitrogen Attune NXT cytometer (ThermoFisher Scientific, Waltham, MA). To assess the mechanism of uptake of the PMAG NPs, the RAW 264.7 macrophages were pretreated with D-mannose at a concentration of 12.5mM for 2 h before NP incubation to block MMR.

Fluorescence microscopy was performed using an Agilent Cytation 10 (Santa Clara, CA) to image NP internalization by macrophages. The cells were seeded in a 12-well plate at a density of 200,000 cells/well and allowed to adhere for 24 h. The cells were then treated with 250 μg/mL of NP solution in media for 2 h, washed with PBS three times, and then fixed with formaldehyde before adding mounting medium with DAPI. Images were taken at 20x magnification.

4.12. In vivo TAM internalization

4T1 breast cancer cells (1 x 10^6) were injected into the mammary fat pad of 4–6-week-old immune-competent BALB/c mice and allowed to grow to a volume of about 200 mm^3. The mice were divided into two groups of five and were administered DiD-loaded PMAM NPs intratumorally at an NP concentration of 25 mg/kg (1 mg/kg DiD) or untreated for control. After 24 h, the mice were sacrificed, and the tumors were harvested and used to produce single-cell suspensions. Flow cytometry was used to assess internalization by TAMs. A flowchart of the gating strategy is presented in **Figure S7**. Cells were first isolated from debris using a side scatter (SSC-A) vs forward scatter (FSC-A) density plot. A density plot of the FSC-H vs FSC-A was then plotted to isolate single cells from doublets and triplets. SSC-A vs EPCAM was then plotted to determine the tumor cell population. The low-expressing EPCAM cells were gated, and a plot of SSC-A vs F4/80 was plotted to determine the TAM population.

4.13. Therapeutic efficacy

4T1 breast tumors were established similarly to the preceding section and allowed to grow to a volume of 100 mm^3. The mice were divided into three groups of five. For three consecutive weeks, the three treatment groups were given intratumoral administrations of UNC2025-loaded PMAM NPs (50 μL of 75 mg/kg NP solution containing 3 mg/kg UNC2025), intraperitoneal administrations of free UNC2025 (50 μL of 3 mg/kg UNC2025), or saline (50 μL) as control. The tumor volumes were measured twice a week for the duration of the experiment. The tumor volumes were calculated using the formula $0.5 \times (Width)^2 \times Length$. At the endpoint, the mice were sacrificed, and the tumors were harvested and weighed. Retro-orbital blood collection was performed at the time of sacrifice and the blood was transferred into EDTA-coated tubes and

analyzed for the count of blood components such as RBC, WBC, and HGB. The serum was harvested from whole blood by clotting at RT and centrifuged at 1500xg for 10 min. Serum chemistry parameters were analyzed as previously reported.[64]

4.14. Statistical analysis

The data presented were the means of each data group with corresponding standard error of the mean (SEM) unless indicated otherwise. The means of two data groups were compared using the unpaired Student's t-test to determine statistical significance ($p<0.05$). The means of three or more data groups were analyzed using one-way ANOVA to determine statistical significance, with Tukey's post hoc procedure to determine the statistical significance between specific treatment groups ($p<0.05$).

Supporting Information

Additional experimental data, including chemical characterization data and flow cytometry histograms

Acknowledgments

The research reported in this publication was supported by an Institutional Development Award (IDeA) from the National Institute of General Medical Sciences of the National Institutes of Health under awards P20GM103460 and P20GM103476. This material is based upon work supported by the National Science Foundation under Grant CAREER 2141666. The researchers acknowledge the core facilities of the Center for Nano-Bio Interactions supported under Grant #2414442 of the NSF EPSCOR program. This material is based upon work supported by the American Cancer

Society under Grant RSG-21-114-01-MM. The authors thank the University of Mississippi's Department of Biochemistry and Chemistry for their FTIR facilities. The authors also thank the Institute for Imaging and Analytical Technology (I2AT) at Mississippi State University for their help with TEM characterization. The I2AT is supported by various NIH, NSF, DoE, DoD awards and University funding.

References

(1) Dunn, G. P.; Bruce, A. T.; Ikeda, H.; Old, L. J.; Schreiber, R. D. Cancer Immunoediting: From Immuno-Surveillance to Tumor Escape. *Nat. Immunol.* 2002. (http://www.nature.com/natureimmunology).

(2) Topalian, S. L.; Drake, C. G.; Pardoll, D. M. Immune Checkpoint Blockade: A Common Denominator Approach to Cancer Therapy. *Cancer Cell*. Cell Press April 13, 2015, pp 450–461. https://doi.org/10.1016/j.ccell.2015.03.001.

(3) Postow, M. A.; Callahan, M. K.; Wolchok, J. D. Immune Checkpoint Blockade in Cancer Therapy. J. Clin. Oncol. 2015, 33, 1974–1982. DOI: 10.1200/JCO.2014.59.4358.

(4) Robert, C. A Decade of Immune-Checkpoint Inhibitors in Cancer Therapy. *Nat. Commun.* 2020, *11*, Article 1. DOI: 10.1038/s41467-020-17670-y.

(5) Shofolawe-Bakare, O. T.; Stokes, L. D.; Hossain, M.; Smith, A. E.; Werfel, T. A. Immunostimulatory Biomaterials to Boost Tumor Immunogenicity. *Biomater. Sci.* 2020, *8*, 5516–5537. DOI: 10.1039/d0bm01183e.

(6) Darvin, P.; Toor, S. M.; Sasidharan Nair, V.; Elkord, E. Immune Checkpoint Inhibitors: Recent Progress and Potential Biomarkers. *Exp. Mol. Med.* 2018, *50*, Article 1. DOI: 10.1038/s12276-018-0191-1.

(7) Werfel, T. A.; Cook, R. S. Efferocytosis in the Tumor Microenvironment. *Semin. Immunopathol.* 2018, *40*, 545–554. DOI: 10.1007/s00281-018-0698-5.

(8) Qiu, H.; Shao, Z.; Wen, X.; Liu, Z.; Chen, Z.; Qu, D.; Ding, X.; Zhang, L. Efferocytosis: An Accomplice of Cancer Immune Escape. *Biomed. Pharmacother.* 2023, *157*, 115540. DOI: 10.1016/j.biopha.2023.115540.

(9) Doran, A. C.; Yurdagul, A.; Tabas, I. Efferocytosis in Health and Disease. *Nat. Rev. Immunol.* 2020, *20*, 254–267. DOI: 10.1038/s41577-019-0240-6.

(10) Lin, J.; Xu, A.; Jin, J.; Zhang, M.; Lou, J.; Qian, C.; Zhu, J.; Wang, Y.; Yang, Z.; Li, X.; Yu, W.; Liu, B.; Tao, H. MerTK-Mediated Efferocytosis Promotes Immune Tolerance and Tumor Progression in Osteosarcoma through Enhancing M2 Polarization and PD-L1 Expression. *Oncoimmunology* 2022, *11*, Article 1. DOI: 10.1080/2162402X.2021.2024941.

(11) Christofides, A.; Strauss, L.; Yeo, A.; Cao, C.; Charest, A.; Boussiotis, V. A. The Complex Role of Tumor-Infiltrating Macrophages. *Nature Immunol*. 2022, pp 1148–1156, https://doi.org/10.1038/s41590-022-01267-2.

(12) Myers, K. V.; Amend, S. R.; Pienta, K. J. Targeting Tyro3, Axl and MerTK (TAM Receptors): Implications for Macrophages in the Tumor Microenvironment. *Mol. Cancer*. 2019, https://doi.org/10.1186/s12943-019-1022-2.

(13) Yang, M.; Liu, J.; Piao, C.; Shao, J.; Du, J. ICAM-1 Suppresses Tumor Metastasis by Inhibiting Macrophage M2 Polarization through Blockade of Efferocytosis. *Cell Death Dis.* **2015**, *6* (6). https://doi.org/10.1038/cddis.2015.144.

(14) Tajbakhsh, A.; Gheibi hayat, S. M.; Movahedpour, A.; Savardashtaki, A.; Loveless, R.; Barreto, G. E.; Teng, Y.; Sahebkar, A. The Complex Roles of Efferocytosis in Cancer Development, Metastasis, and Treatment. *Biomed. and Pharmacother*. 2021, https://doi.org/10.1016/j.biopha.2021.111776.

(15) Cook, R. S.; Jacobsen, K. M.; Wofford, A. M.; DeRyckere, D.; Stanford, J.; Prieto, A. L.; Redente, E.; Sandahl, M.; Hunter, D. M.; Strunk, K. E.; Graham, D. K.; Earp, H. S. MerTK Inhibition in Tumor Leukocytes Decreases Tumor Growth and Metastasis. *J. Clin. Inv.* **2013**, *123* (8), 3231–3242. https://doi.org/10.1172/JCI67655.

(16) Yan, D.; Earp, H. S.; Deryckere, D.; Graham, D. K. Targeting Mertk and Axl in Egfr Mutant Non-Small Cell Lung Cancer. *Cancers*. 2021. https://doi.org/10.3390/cancers13225639.

(17) Lahey, K. C.; Gadiyar, V.; Hill, A.; Desind, S.; Wang, Z.; Davra, V.; Patel, R.; Zaman, A.; Calianese, D.; Birge, R. B. Mertk: An Emerging Target in Cancer Biology and Immuno-Oncology. *Inter. Rev. Cell Mol. Bio.*, 2022, Vol. 368, pp 35–59. https://doi.org/10.1016/bs.ircmb.2022.04.004.

(18) Mai Itoh, Y. K.; Tohda, S. Effects of MERTK Inhibitors UNC569 and UNC1062 on the Growth of Acute Myeloid Leukaemia Cells. *Anticancer Res* **2018**, *38* (1), 199–204. https://doi.org/10.21873/anticanres.12208.

(19) Dutta, B.; Barick, K. C.; Hassan, P. A. Recent Advances in Active Targeting of Nanomaterials for Anticancer Drug Delivery. *Adv. Coll. Interfacial Sci.*, 2021, https://doi.org/10.1016/j.cis.2021.102509.

(20) Ngambenjawong, C.; Gustafson, H. H.; Pun, S. H. Progress in Tumor-Associated Macrophage (TAM)-Targeted Therapeutics. *Adv. Drug Del. Rev*. 2017, pp 206–221. https://doi.org/10.1016/j.addr.2017.04.010.

(21) Singh, Y.; Pawar, V. K.; Meher, J. G.; Raval, K.; Kumar, A.; Shrivastava, R.; Bhadauria, S.; Chourasia, M. K. Targeting Tumor Associated Macrophages (TAMs) via Nanocarriers. *J. Contr. Rel*., 2017, pp 92–106. https://doi.org/10.1016/j.jconrel.2017.03.395.

(22) Jaynes, J. M.; Sable, R.; Ronzetti, M.; Bautista, W.; Knotts, Z.; Abisoye-Ogunniyan, A.; Li, D.; Calvo, R.; Dashnyam, M.; Singh, A.; Guerin, T.; White, J.; Ravichandran, S.; Kumar, P.; Talsania, K.; Chen, V.; Ghebremedhin, A.; Karanam, B.; Salam, A. Bin; Amin, R.; Odzorig, T.; Aiken, T.; Nguyen, V.; Bian, Y.; Zarif, J. C.; de Groot, A. E.; Mehta, M.; Fan, L.; Hu, X.; Simeonov, A.; Pate, N.; Abu-Asab,

M.; Ferrer, M.; Southall, N.; Ock, C. Y.; Zhao, Y.; Lopez, H.; Kozlov, S.; de Val, N.; Yates, C. C.; Baljinnyam, B.; Marugan, J.; Rudloff, U. Mannose Receptor (CD206) Activation in Tumor-Associated Macrophages Enhances Adaptive and Innate Antitumor Immune Responses. *Sci Transl Med,* **2020**, *12* (530). https://doi.org/10.1126/scitranslmed.aax6337.

(23) Guo, Y.; Feinberg, H.; Conroy, E.; Mitchell, D. A.; Alvarez, R.; Blixt, O.; Taylor, M. E.; Weis, W. I.; Drickamer, K. Structural Basis for Distinct Ligand-Binding and Targeting Properties of the Receptors DC-SIGN and DC-SIGNR. *Nat Struct Mol Biol* **2004**, *11* (7), 591–598. https://doi.org/10.1038/nsmb784.

(24) Glass, E. B.; Hoover, A. A.; Bullock, K. K.; Madden, M. Z.; Reinfeld, B. I.; Harris, W.; Parker, D.; Hufnagel, D. H.; Crispens, M. A.; Khabele, D.; Rathmell, W. K.; Rathmell, J. C.; Wilson, A. J.; Giorgio, T. D.; Yull, F. E. Stimulating TAM-Mediated Anti-Tumor Immunity with Mannose-Decorated Nanoparticles in Ovarian Cancer. *BMC Cancer* **2022**, *22* (1). https://doi.org/10.1186/s12885-022-09612-2.

(25) Zhang, F.; Parayath, N. N.; Ene, C. I.; Stephan, S. B.; Koehne, A. L.; Coon, M. E.; Holland, E. C.; Stephan, M. T. Genetic Programming of Macrophages to Perform Anti-Tumor Functions Using Targeted MRNA Nanocarriers. *Nat Commun* **2019**, *10* (1). https://doi.org/10.1038/s41467-019-11911-5.

(26) Zhu, S.; Niu, M.; O'Mary, H.; Cui, Z. Targeting of Tumor-Associated Macrophages Made Possible by PEG-Sheddable, Mannose-Modified Nanoparticles. *Mol Pharm* **2013**, *10* (9), 3525–3530. https://doi.org/10.1021/mp400216r.

(27) Stenzel, M. H. Glycopolymers for Drug Delivery: Opportunities and Challenges. *Macromolecules*, 2022, pp 4867–4890. https://doi.org/10.1021/acs.macromol.2c00557.

(28) Yoo, D.; Whang, C. H.; Hong, J.; Kim, D.; Prayogo, M. C.; Son, Y.; Jung, W.; Lee, S.; Lee, H. S.; Jon, S. Anti-Inflammatory Glycocalyx-Mimicking Nanoparticles for Colitis Treatment: Construction and In Vivo Evaluation. *Ang. Chemie – Int. Ed.* **2023**, *62* (34). https://doi.org/10.1002/anie.202304815.

(29) Song, E. H.; Manganiello, M. J.; Chow, Y. H.; Ghosn, B.; Convertine, A. J.; Stayton, P. S.; Schnapp, L. M.; Ratner, D. M. In Vivo Targeting of Alveolar Macrophages via RAFT-Based Glycopolymers. *Biomaterials* **2012**, *33* (28), 6889–6897. https://doi.org/10.1016/j.biomaterials.2012.06.025.

(30) Yu, H.; Zou, Y.; Wang, Y.; Huang, X.; Huang, G.; Sumer, B. D.; Boothman, D. A.; Gao, J. Overcoming Endosomal Barrier by Amphotericin B-Loaded Dual PH-Responsive PDMA- b-PDPA Micelleplexes for SiRNA Delivery. *ACS Nano* **2011**, *5* (11), 9246–9255. https://doi.org/10.1021/nn203503h.

(31) Garrett, W. S.; Mellman, I. *Studies of Endocytosis*; 2001. https://doi.org/10.1016/B978-0-12-455851-9.50055-9.

(32) Lopukhov, A. V.; Yang, Z.; Haney, M. J.; Bronich, T. K.; Sokolsky-Papkov, M.; Batrakova, E. V.; Klyachko, N. L.; Kabanov, A. V. Mannosylated Cationic Copolymers for Gene Delivery to Macrophages. *Macromol Biosci* **2021**, *21* (4). https://doi.org/10.1002/mabi.202000371.

(33) Silva-Santana, G.; Bax, J. C.; Fernandes, D. C. S.; Bacellar, D. T. L.; Hooper, C.; Dias, A. A. S. O.; Silva, C. B.; de Souza, A. M.; Ramos, S.; Santos, R. A.; Pinto, T. R.; Ramão, M. A.; Mattos-Guaraldi,

A. L. Clinical Hematological and Biochemical Parameters in Swiss, BALB/c, C57BL/6 and B6D2F1 Mus Musculus. *Animal Model Exp Med* **2020**, *3* (4), 304–315. https://doi.org/10.1002/ame2.12139.

(34) Chen, W.; Wang, W.; Zhou, L.; Zhou, J.; He, L.; Li, J.; Xu, X.; Wang, J.; Wang, L. Elevated AST/ALT Ratio Is Associated with All-Cause Mortality and Cancer Incident. *J Clin Lab Anal* **2022**, *36* (5). https://doi.org/10.1002/jcla.24356.

(35) Fernandes, D. P.; Pimentel, M. M. L.; Dos Santos, F. A.; Praxedes, É. A.; DE BRITO, P. D.; Lima, M. A.; Lelis, I. C. N. G.; de Macedo, M. F.; Bezerra, M. B. Hematological and Biochemical Profile of BALB/c Nude and C57BL/6 SCID Female Mice after Ovarian Xenograft. *An Acad Bras Cienc* **2018**, *90* (4), 3941–3948. https://doi.org/10.1590/0001-3765201820180586.

(36) Lee, J.; Kim, D.; Son, E.; Yoo, S. J.; Sa, J. K.; Shin, Y. J.; Yoon, Y.; Nam, D. H. Pharmacokinetics, Biodistribution, and Toxicity Evaluation of Anti-SEMA3A (F11) in in Vivo Models. *Anticancer Res* **2018**, *38* (5), 2803–2810. https://doi.org/10.21873/anticanres.12524.

(37) De Souza, C. M.; Araújo e Silva, A. C.; De Jesus Ferraciolli, C.; Moreira, G. V.; Campos, L. C.; Dos Reis, D. C.; Lopes, M. T. P.; Ferreira, Mô. A. N. D.; Andrade, S. P.; Cassali, G. D. Combination Therapy with Carboplatin and Thalidomide Suppresses Tumor Growth and Metastasis in 4T1 Murine Breast Cancer Model. *Biomed. and Pharmacother.* **2014**, *68* (1), 51–57. https://doi.org/10.1016/j.biopha.2013.08.004.

(38) Li, K.; Lu, L.; Xue, C.; Liu, J.; He, Y.; Zhou, J.; Xia, Z.; Dai, L.; Luo, Z.; Mao, Y.; Cai, K. Polarization of Tumor-Associated Macrophage Phenotype: Via Porous Hollow Iron Nanoparticles for Tumor Immunotherapy in Vivo. *Nanoscale* **2020**, *12* (1), 130–144. https://doi.org/10.1039/c9nr06505a.

(39) Tang, X.; Mo, C.; Wang, Y.; Wei, D.; Xiao, H. Anti-Tumour Strategies Aiming to Target Tumour-Associated Macrophages. *Immunology*. 2013, pp 93–104. https://doi.org/10.1111/imm.12023.

(40) Fu, L. Q.; Du, W. L.; Cai, M. H.; Yao, J. Y.; Zhao, Y. Y.; Mou, X. Z. The Roles of Tumor-Associated Macrophages in Tumor Angiogenesis and Metastasis. *Cell. Immunology*., 2020. https://doi.org/10.1016/j.cellimm.2020.104119.

(41) Chaib, M.; Chauhan, S. C.; Makowski, L. Friend or Foe? Recent Strategies to Target Myeloid Cells in Cancer. *Front. Cell Dev. Bio*., 2020. https://doi.org/10.3389/fcell.2020.00351.

(42) Wang, B.; Zhang, W.; Zhou, X.; Liu, M.; Hou, X.; Cheng, Z.; Chen, D. Development of Dual-Targeted Nano-Dandelion Based on an Oligomeric Hyaluronic Acid Polymer Targeting Tumor-Associated Macrophages for Combination Therapy of Non-Small Cell Lung Cancer. *Drug Deliv* **2019**, *26* (1), 1265–1279. https://doi.org/10.1080/10717544.2019.1693707.

(43) Gao, W.; Chan, J. M.; Farokhzad, O. C. PH-Responsive Nanoparticles for Drug Delivery. *Mol Pharm*., 2010, pp 1913–1920. https://doi.org/10.1021/mp100253e.

(44) Rushworth, J. L.; Montgomery, K. S.; Cao, B.; Brown, R.; Dibb, N. J.; Nilsson, S. K.; Chiefari, J.; Fuchter, M. J. Glycosylated Nanoparticles Derived from RAFT Polymerization for Effective Drug Delivery to Macrophages. *ACS Appl Bio Mater* **2020**, *3* (9), 5775–5786. https://doi.org/10.1021/acsabm.0c00529.

(45) Yu, S. S.; Lau, C. M.; Barham, W. J.; Onishko, H. M.; Nelson, C. E.; Li, H.; Smith, C. A.; Yull, F. E.; Duvall, C. L.; Giorgio, T. D. Macrophage-Specific RNA Interference Targeting via “Click”, Mannosylated Polymeric Micelles. *Mol Pharm* **2013**, *10* (3), 975–987. https://doi.org/10.1021/mp300434e.

(46) Al-Ghananeem, A. M.; Malkawi, A. H.; Muammer, Y. M.; Balko, J. M.; Black, E. P.; Mourad, W.; Romond, E. Intratumoral Delivery of Paclitaxel in Solid Tumor from Biodegradable Hyaluronan Nanoparticle Formulations. *AAPS PharmSciTech* **2009**, *10* (2), 410–417. https://doi.org/10.1208/s12249-009-9222-5.

(47) Cai, Z.; Chattopadhyay, N.; Yang, K.; Kwon, Y. L.; Yook, S.; Pignol, J. P.; Reilly, R. M. 111In-Labeled Trastuzumab-Modified Gold Nanoparticles Are Cytotoxic in Vitro to HER2-Positive Breast Cancer Cells and Arrest Tumor Growth in Vivo in Athymic Mice after Intratumoral Injection. *Nucl Med Biol* **2016**, *43* (12), 818–826. https://doi.org/10.1016/j.nucmedbio.2016.08.009.

(48) Zuo, C.; Zou, Y.; Gao, G.; Sun, L.; Yu, B.; Guo, Y.; Wang, X.; Han, M. Photothermal Combined with Intratumoral Injection of Annonaceous Acetogenin Nanoparticles for Breast Cancer Therapy. *Colloids Surf B Biointerfaces* **2022**, *213*. https://doi.org/10.1016/j.colsurfb.2022.112426.

(49) Yun, W. S.; Kim, J.; Lim, D. K.; Kim, D. H.; Jeon, S. I.; Kim, K. Recent Studies and Progress in the Intratumoral Administration of Nano-Sized Drug Delivery Systems. *Nanomaterials*., 2023. https://doi.org/10.3390/nano13152225.

(50) Bahmani, B.; Gong, H.; Luk, B. T.; Haushalter, K. J.; DeTeresa, E.; Previti, M.; Zhou, J.; Gao, W.; Bui, J. D.; Zhang, L.; Fang, R. H.; Zhang, J. Intratumoral Immunotherapy Using Platelet-Cloaked Nanoparticles Enhances Antitumor Immunity in Solid Tumors. *Nat Commun* **2021**, *12* (1). https://doi.org/10.1038/s41467-021-22311-z.

(51) Zhang, Y.; Yue, S.; Haag, R.; Sun, H.; Zhong, Z. An Intelligent Cell-Selective Polymersome-DM1 Nanotoxin toward Triple Negative Breast Cancer. *J. Contr. Rel.* **2021**, *340*, 331–341. https://doi.org/10.1016/j.jconrel.2021.11.014.

(52) Cabral, H.; Kinoh, H.; Kataoka, K. Tumor-Targeted Nanomedicine for Immunotherapy. *Acc Chem Res* **2020**, *53* (12), 2765–2776. https://doi.org/10.1021/acs.accounts.0c00518.

(53) Cheng, F.; Su, T.; Zhou, S.; Liu, X.; Yang, S.; Lin, S.; Guo, W.; Zhu, G. Single-Dose Injectable Nanovaccine-in-Hydrogel for Robust Immunotherapy of Large Tumors with Abscopal Effect. Sci Adv. 2023. Jul 14;9(28) doi: 10.1126/sciadv.ade6257

(54) Buss, C. G.; Bhatia, S. N. Nanoparticle Delivery of Immunostimulatory Oligonucleotides Enhances Response to Checkpoint Inhibitor Therapeutics. *Proceedings of the National Academy of Science* **2020**, *117* (24), 13428–13436.

(55) Wu, Y.; Wang, C.; Yan, Y.; Hao, Y.; Liu, B.; Dong, Z.; Chen, M.; Zhu, Y.; Liu, N.; Feng, L.; Liu, Z. Efferocytosis Nanoinhibitors to Promote Secondary Necrosis and Potentiate the Immunogenicity of Conventional Cancer Therapies for Improved Therapeutic Benefits. *ACS Nano* **2023**, *17* (18), 18089–18102. https://doi.org/10.1021/acsnano.3c04884.

(56) Zhang, J. Y.; Chen, F. M.; Li, Y. X.; Duan, Q. J.; Wu, C.; Zheng, S. J.; Leong, K. W.; Shao, D.; Du, J. Z. Leveraging Efferocytosis Blockade for Improved Cancer Chemo-Immunotherapy through Synchronized Release of Doxorubicin and BMS777607 Confined within Tailored Mesoporous Silica Nanoparticles. *Nano Today* **2023**, *53*. https://doi.org/10.1016/j.nantod.2023.102039.

(57) Wu, J.; Frady, L. N.; Bash, R. E.; Cohen, S. M.; Schorzman, A. N.; Su, Y. T.; Irvin, D. M.; Zamboni, W. C.; Wang, X.; Frye, S. V.; Ewend, M. G.; Sulman, E. P.; Gilbert, M. R.; Earp, H. S.; Miller, C. R. MerTK as a Therapeutic Target in Glioblastoma. *Neuro Oncol* **2018**, *20* (1), 92–102. https://doi.org/10.1093/neuonc/nox111.

(58) De Lombaerde, E.; De Wever, O.; De Geest, B. G. Delivery Routes Matter: Safety and Efficacy of Intratumoral Immunotherapy. *Biochimica et Biophysica Acta – Rev. Cancer*, 2021. https://doi.org/10.1016/j.bbcan.2021.188526.

(59) Wei, Y.; Quan, L.; Zhou, C.; Zhan, Q. Factors Relating to the Biodistribution & Clearance of Nanoparticles & Their Effects on in Vivo Application. *Nanomedicine*. 2018, pp 1495–1512. https://doi.org/10.2217/nnm-2018-0040.

(60) Oliveira, C. L.; Veiga, F.; Varela, C.; Roleira, F.; Tavares, E.; Silveira, I.; Ribeiro, A. J. Characterization of Polymeric Nanoparticles for Intravenous Delivery: Focus on Stability. *Colloids Surf B Biointerfaces* **2017**, *150*, 326–333. https://doi.org/10.1016/j.colsurfb.2016.10.046.

(61) Hu, Y. Q.; Kim, M. S.; Kim, B. S.; Lee, D. S. Synthesis and PH-Dependent Micellization of 2-(Diisopropylamino)Ethyl Methacrylate Based Amphiphilic Diblock Copolymers via RAFT Polymerization. *Polymer (Guildf)* **2007**, *48* (12), 3437–3443. https://doi.org/10.1016/j.polymer.2007.04.011.

(62) Pearson, S.; Allen, N.; Stenzel, M. H. Core-Shell Particles with Glycopolymer Shell and Polynucleoslde Core via RAFT: From Micelles to Rods. *J Polym Sci A Polym Chem* **2009**, *47* (6), 1706–1723. https://doi.org/10.1002/pola.23275.

(63) Shofolawe-Bakare, O. T.; de Mel, J. U.; Mishra, S. K.; Hossain, M.; Hamadani, C. M.; Pride, M. C.; Dasanayake, G. S.; Monroe, W.; Roth, E. W.; Tanner, E. E. L.; Doerksen, R. J.; Smith, A. E.; Werfel, T. A. ROS-Responsive Glycopolymeric Nanoparticles for Enhanced Drug Delivery to Macrophages. *Macromol Biosci* **2022**, *22* (12). https://doi.org/10.1002/mabi.202200281.

(64) Mohammad, S. A.; Toragall, V. B.; Fortenberry, A.; Shofolawe-Bakare, O.; Sulochana, S.; Heath, K.; Owolabi, I.; Tassin, G.; Flynt, A. S.; Smith, A. E.; Werfel, T. Postpolymerization Modification of Poly(2-Vinyl-4,4-Dimethyl Azlactone) as a Versatile Strategy for Drug Conjugation and Stimuli-Responsive Release. *Biomacromolecules* **2024**. https://doi.org/10.1021/acs.biomac.4c00181.